












Article

Propagation of Perturbations in the Lower and Upper Atmosphere over the Central Mediterranean, Driven by the 15 January 2022 Hunga Tonga-Hunga Ha'apai Volcano Explosion

Paolo Madonia ^{1,*}, Alessandro Bonaccorso ¹, Alessandro Bonforte ¹, Ciro Buonocunto ², Andrea Cannata ^{1,3}, Luigi Carleo ¹, Claudio Cesaroni ⁴, Gilda Currenti ¹, Sofia De Gregorio ⁵, Bellina Di Lieto ², Marco Guerra ⁴, Massimo Orazi ², Luigi Pasotti ⁶, Rosario Peluso ², Michael Pezzopane ⁴, Vito Restivo ⁶, Pierdomenico Romano ², Mariangela Sciotto ¹ and Luca Spogli ⁴

- ¹ Istituto Nazionale di Geofisica e Vulcanologia, Osservatorio Etneo, 95125 Catania, Italy
² Istituto Nazionale di Geofisica e Vulcanologia, Osservatorio Vesuviano, 80124 Napoli, Italy
³ Dipartimento Di Scienze Biologiche, Geologiche E Ambientali-Sezione Di Scienze Della Terra, Università Degli Studi Di Catania, 95129 Catania, Italy
⁴ Istituto Nazionale di Geofisica e Vulcanologia, Sezione Roma 2, 00143 Roma, Italy
⁵ Istituto Nazionale di Geofisica e Vulcanologia, Sezione di Palermo, 90146 Palermo, Italy
⁶ Servizio Informativo Agrometeorologico Siciliano, 90135 Palermo, Italy
* Correspondence: paolo.madonia@ingv.it



Citation: Madonia, P.; Bonaccorso, A.; Bonforte, A.; Buonocunto, C.; Cannata, A.; Carleo, L.; Cesaroni, C.; Currenti, G.; De Gregorio, S.; Di Lieto, B.; et al. Propagation of Perturbations in the Lower and Upper Atmosphere over the Central Mediterranean, Driven by the 15 January 2022 Hunga Tonga-Hunga Ha'apai Volcano Explosion. *Atmosphere* **2023**, *14*, 65. <https://doi.org/10.3390/atmos14010065>

Academic Editors: Goderdzi Didebulidze and Sergey P. Kshevetskii

Received: 7 December 2022

Revised: 23 December 2022

Accepted: 24 December 2022

Published: 29 December 2022



Copyright: © 2022 by the authors. Licensee MDPI, Basel, Switzerland. This article is an open access article distributed under the terms and conditions of the Creative Commons Attribution (CC BY) license (<https://creativecommons.org/licenses/by/4.0/>).

Abstract: The Hunga Tonga-Hunga Ha'apai volcano (Pacific Ocean) generated a cataclysmic explosion on 15 January 2022, triggering several atmospheric disturbances at a global scale, as a huge increase in the total electron content (TEC) in the ionosphere, and a pressure wave travelling in the troposphere. We collected and analysed data over the Mediterranean to study these disturbances, and in particular, (i) data from the barometric and infrasonic stations installed on Italian active volcanoes by the Istituto Nazionale di Geofisica e Vulcanologia (INGV) for investigating the tropospheric pressure waves; (ii) barometric data from the INGV-TROPOMAG and SIAS (Sicilian Agro-meteorological Information System) networks, for investigating the interaction between the orography and pressure waves; (iii) ionograms from the Advanced Ionospheric Sounder-INGV ionosonde at Gibilmanna (Sicily, Italy); (iv) data from the RING (Rete Italiana Integrata GNSS) network, to retrieve the ionospheric TEC; (v) soil CO₂ flux data from the INGV surveillance network of Vulcano Island. The analysis of the ground-level barometric data highlights that pressure waves were reflected and diffracted by the topographic surface, creating a complex space–time dynamic of the atmospheric disturbances travelling over Sicily, driven by the interference among the different wavefronts. The ionograms show that a medium-scale travelling ionospheric disturbance (MSTID), with a horizontal wavelength of about 220 km and a period of about 35 min, propagated through the ionospheric plasma in the correspondence of the first barometric variations. Moreover, comparing detrended TEC and barometric data, we further confirmed the presence of the aforementioned MSTID together with its close relation to the tropospheric disturbance.

Keywords: atmospheric pressure; GNSS; lithosphere–atmosphere–ionosphere coupling; soil degassing; travelling ionospheric disturbances; troposphere

1. Introduction

Hunga Tonga-Hunga Ha'apai, hereafter referred to as Hunga, is a mainly submarine volcano located in the south-western Pacific Ocean (20°33' S, 175°23' W), whose emerged part comprises two small uninhabited islets (about 2 km long each, with a maximum altitude of 110 m), named Hunga Tonga and Hunga Ha'apai. Hunga volcano produced a series of large eruptions about 900 years ago, followed by numerous less energetic events, the penultimate of which formed a new island in 2014/15 [1].

The most recent eruption of 2022 culminated in a cataclysmic series of explosions at about 04:00 UTC on 15 January, the most energetic volcanic explosion ever to have occurred in the last 138 years (comparable to those of Pinatubo in 1991 and Krakatau in 1883). It generated a volcanic plume of more than 58 km high and triggered several disturbances in fluid Earth at a global scale [2].

These disturbances included (i) tsunami waves recorded beyond the Pacific Ocean [3]; (ii) a huge amount of water vapour injected into the atmosphere [4]; (iii) a pressure wave travelling in the troposphere at 305 m s^{-1} , which triggered downward ground vibrations and, upward, secondary total electron content (TEC) perturbations, delayed by 12 min with respect to the positive pressure pulse [5]; (iv) a huge increase in the total electron content (TEC) in the ionosphere, delayed by 12 min with respect to the positive tropospheric pressure pulse [5] and followed by a strong, long-lasting depletion [6]. In the present study, attention was focused on the relationship between the tropospheric pressure wave, its interaction with orography, and the ionospheric disturbances, with a focus on the South Mediterranean area.

Specifically, concerning ionospheric disturbances, Astafyeva [7] has recently reviewed how natural hazards, such as earthquakes, tsunamis and volcanic eruptions, trigger acoustic and gravity waves that propagate upward in the atmosphere and ionosphere.

The propagation of the pressure wave generated by the Hunga explosion has been described by several authors. Chen et al. [5] compared the propagation velocity of the tropospheric pressure enhancement and ionospheric TEC anomalies over Japan and all around China, finding that the latter preceded the former by 12 min. Matoza et al. [8], analysing data from a global multiparametric geophysical network, described the Hunga pressure wave, characterised by complex waveform and spectral characteristics. According to the authors, the pressure disturbance travelled around the Earth as a Lamb wave, with a frequency ranging between 0.3 and 10 mHz, composed of several atmospheric waves, i.e., acoustic and gravity waves. Harrison [9] described the passage of the pressure wave over the United Kingdom, as detected by a barometric meteorological network (10 min acquisition period). The network detected the arrival of the first pulse (from the north) at about 18:00 UTC, followed 6 h later by the second one from the south. Both pulses travelled at a similar speed (315 m s^{-1}) and caused transient pressure anomalies of 0.5 to 1 hPa, initially positive and then negative, whose observation was made easier by settled anticyclonic conditions. The passage of this large pressure disturbance generated additional atmospheric changes across the UK, as the variability of the base height of a low stratus was detected over Reading by a laser ceilometer providing one-minute data. The passage of the Hunga shockwave suddenly rose the cloud base height just before 20:00 UTC, causing an increase in the surface air temperature.

Both Wright et al. [10] and Themens et al. [11] performed a global analysis of the propagation of travelling ionospheric disturbances (TIDs), a proxy of the manifestation of atmospheric waves in the ionosphere [12], associated with the Hunga event. According to their wavelengths, they are classified into three main classes [13]: (i) large-scale TIDs (LSTIDs), with horizontal wavelengths greater than 1000 km and periods ranging from 30 min to 3 h and horizontal phase velocities between 300 and 1000 m/s; (ii) medium-scale TIDs (MSTIDs) with horizontal wavelengths between 100 and 300 km and periods between about 12 min and 1 h and horizontal phase velocities between 100 and 300 m/s; (iii) small-scale TIDs (SSTIDs) with corresponding wavelengths, velocities and periods that are smaller than those of MSTIDs, because they belong to the acoustic branch.

Themens and co-authors [11] found that two distinct LSTIDs, and several subsequent MSTIDs, propagated radially outward from the eruption site. Additionally, Hong et al. [14] reported transient wave-like TEC modulations and intense irregular TEC perturbations over the Korean Peninsula, which occurred about 8 h after the Hunga volcano eruption. Verhulst and co-authors [15] provided a thorough description of the ionospheric disturbances triggered by both the acoustic and gravity waves caused by this eruption over Europe, which was obtained by integrating various instruments covering the region, including

ionosondes and Global Navigation Satellite System (GNSS) receivers for the TEC retrieval. All the reported studies highlighted the plethora of phenomena concurring in the explosion's worldwide propagation, reinforcing the need for a multi-instrumental approach to depict regional and local effects, as we did in our work.

2. Materials and Methods

Data from different networks and sampling rates populated the database of atmospheric pressure: (i) Hourly data from the INGV Palermo office; (ii) half-hourly data from the INGV-TROPOMAG [<https://progetti.ingv.it/en/tropomag/tropomag-project> (accessed on 1 December 2022)] stations of Palermo (ORT and MPL) and Salina island (SMS and MFF); (iii) 5 min data from the SIAS (Sicilian Agro-meteorological Information System) network [<http://www.sias.regione.sicilia.it> (accessed on 1 December 2022)]; (iv) data from the INGV surveillance system of Italian active volcanoes: 50 Hz barometric data from 3 stations (CQUE, SDRO and DRUV) of the dilatometer network of Campi Flegrei, Stromboli and infrasound data from the Mt. Etna ESLN and Campi Flegrei CBAC stations. Dilatometers are instrumented with a Setra 278 absolute microbarometer, which is sensitive to pressure variations from DC to 2 Hz. The ESLN infrasound station is equipped with a GRAS 40 AN (GRAS Sound and Vibration 2020) polarised free field and a low-frequency microphone with a flat frequency response in a range between 1 Hz and 10 kHz (± 1 dB, ± 2 dB from 0.5 Hz to 20 kHz). This station was selected among the others of the network because of its best recording of the Hunga shockwave due to its far location from the summit's active vents (1600 m lower and 7000 m distant from them). The CBAC infrasound station is equipped with an InfraCyrus (INGV, Napoli, Italy) infrasound sensor, which has a frequency response flat enough within ± 3 dB, between 0.07 and 50 Hz [16].

In order to characterise the effects in the ionosphere, the ionospheric parameters retrieved from the ionograms and the TEC from the ground-based GNSS receivers were considered. The ionograms considered for the present study are those recorded by the Advanced Ionospheric Sounder-INGV (AIS-INGV) (INGV, Roma, Italy) ionosonde (GM037), installed at the ionospheric observatory of Gibilmanna (37.9° N, 14.0° E) [17] and available in the Electronic Space Weather upper atmosphere (eSWua) database [18]. The sounding repetition rate and sweeping frequency range of the AIS-INGV ionosonde were set to 15 min and from 1 to 18 MHz, respectively.

Data from the selected Rete Integrata Nazionale GNSS (RING) stations [19] covering the area of interest have been used for retrieving the total electron content (TEC). As described in [20], the retrieval of the TEC along the slant path, connecting a dual-frequency GNSS receiver and each satellite, exploits the dispersive nature of the ionised part of the atmosphere. In order to identify the propagation of wave-like structures in the ionosphere, the TEC data must be detrended. In this regard, we calibrated and verticalized the slant TEC values for each considered radio link through the calibration technique described in depth in [21]. Then, the detrended vertical TEC (dvTEC) is obtained by applying a bandpass filter (5–40 min) to the calibrated verticalized TEC.

Acquired data are completed by measures of soil CO₂ flux from two stations of the INGV-PA Vulcanogas surveillance network, placed at the base of the La Fosse crater at Vulcano Island in the Aeolian archipelago. The soil CO₂ flux was measured hourly with the dynamic concentration method [22]. The locations of the observing stations are reported in Figure 1.

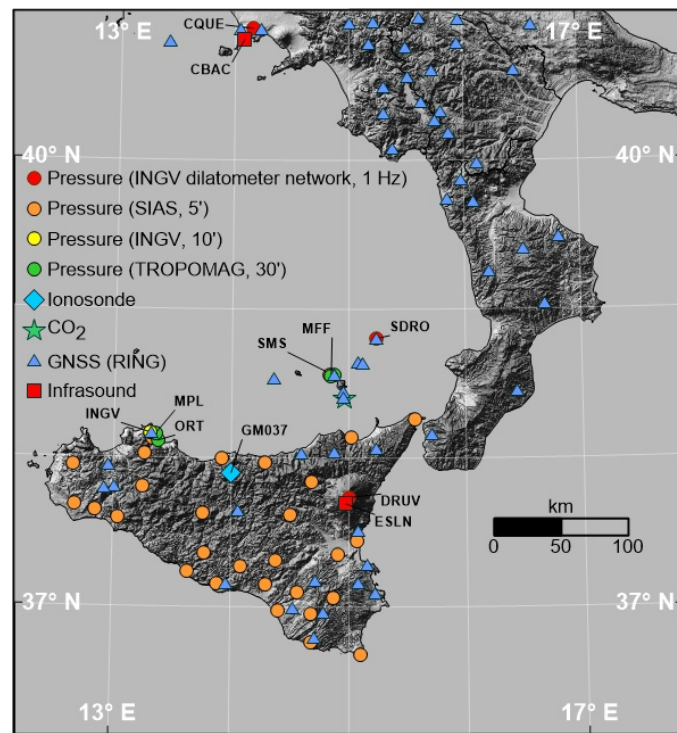


Figure 1. Location of the stations considered in this study, classified for acquired parameter and sampling periodicity.

3. Results

3.1. The Hunga Shockwave over the Mediterranean

The barometric signals, high-pass filtered to a 3 h period in order to remove lower-frequency atmospheric pressure variations, show large amplitude perturbations of a few hPa at all the dilatometer stations, as well as infrasonic signals; the latter recorded significant variations with amplitudes of a few Pa, with a delay of about 1 h, with respect to the former. Signals recorded at Campi Flegrei and Etna are shown in Figure 2.

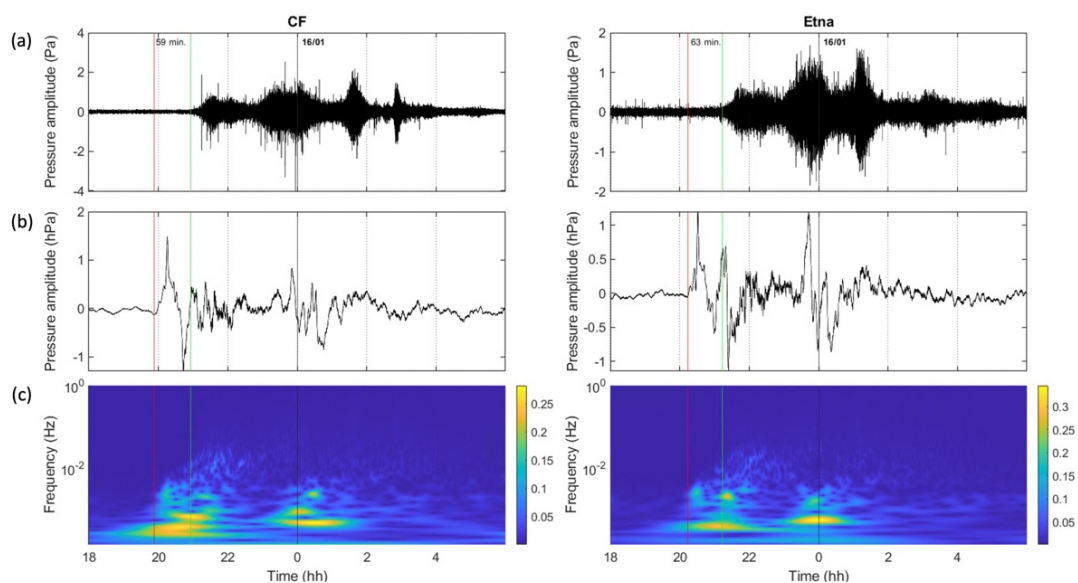


Figure 2. (a) Infrasonic waveforms at Campi Flegrei (CF) and Etna stations showing the acoustic wave arrival; the signal is filtered with a low-pass filter with 10 Hz cutoff. (b) Barometric waveforms, showing the Lamb wave arrival; the signal is filtered with a high-pass filter with 0.093 mHz (3 h period)

cutoff. (c) Continuous wavelet transforms (CWT) of the barometric data show a dispersion line due to lower propagation velocities for higher frequency. The vertical red and green lines indicate the Lamb wave and the acoustic wave arrivals, respectively. In the figure, the delay times (59 and 63 min for CF and Etna, respectively) between Lamb and acoustic wave arrivals are reported.

Both barometric signals record the arrival of a low-frequency wave (4.5 mHz) at 19:55 and at 20:13 at Campi Flegrei and Etna, respectively. The frequency content and the arrival time, indicative of an average velocity propagation of about 310 m/s from Hunga, are associated with the Lamb wave. With a delay of about 1 h, the infrasonic signals mark the arrival of higher-frequency waves that fall into the sensor frequency band (above about 0.2 Hz). The Continuous Wavelet Transform (CWT) shows a clear dispersion line due to the lower propagation velocities for higher frequencies. This time–frequency pattern is in agreement with the dispersion line reported in the literature [23,24], where lower frequencies are associated with acoustic-gravity modes and higher frequencies with acoustic modes

3.2. Lower Atmosphere Response

As discussed in the methods, with the exception of the high frequency (50 Hz) barometers of the INGV dilatometer network, pressure data were acquired by all other instruments with sampling periods of 5 (SIAS), 10 (INGV) and 30 (TROPOMAG) minutes. Figure 3 illustrates the related signals acquired in Palermo (Figure 1), where the different types of instruments were operating; arrival times of the first and second passages of the shockwaves travelling along the short and long (antipodal, not recognisable in the second passage) ranges are also reported.

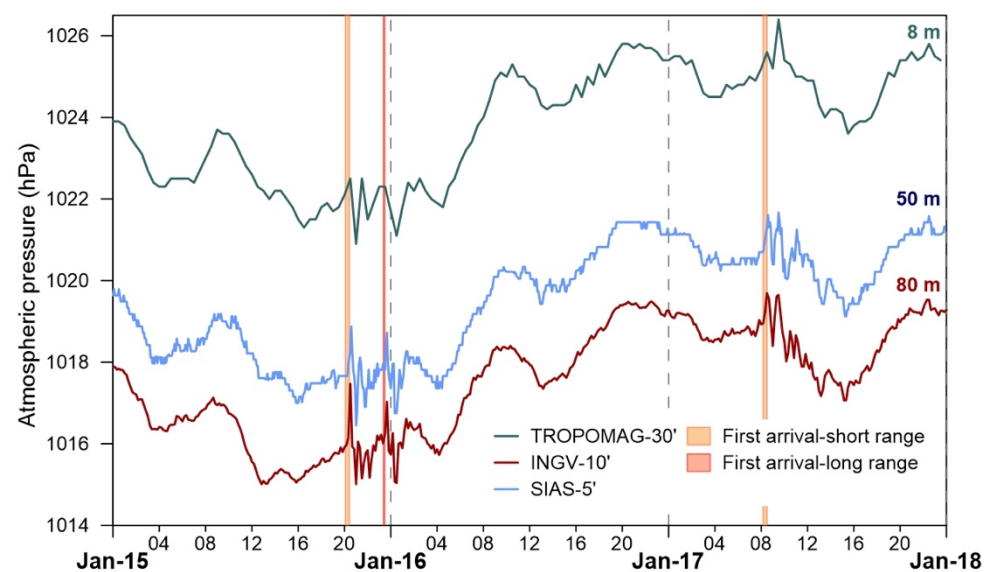


Figure 3. Barometric signals, sampled at 5, 10 and 30 min by different stations located in the city of Palermo (Figure 1). The numbers on the right represent the elevation above sea level of the stations. Orange vertical bars indicate the first arrival of the first and second passage of the shockwave travelling along the short range, the red one the passage of the shockwave along the long (antipodal) range.

Anomalous pressure variations are visible in the 30' signal; however, its dynamics are completely lost, and the antipodal signal of the first passage is not recognisable. Both the 10' and 5' signals provide a more realistic representation of the shockwave passages, without appreciable differences in the timing of the first arrivals, but with a better definition of the higher frequency content in the 5' one, as expected. A different approach for identifying the anomalous transients is the analysis of the first time derivative of the pressure signal, reported in Figure 4a for the Palermo station (5' acquisition period).

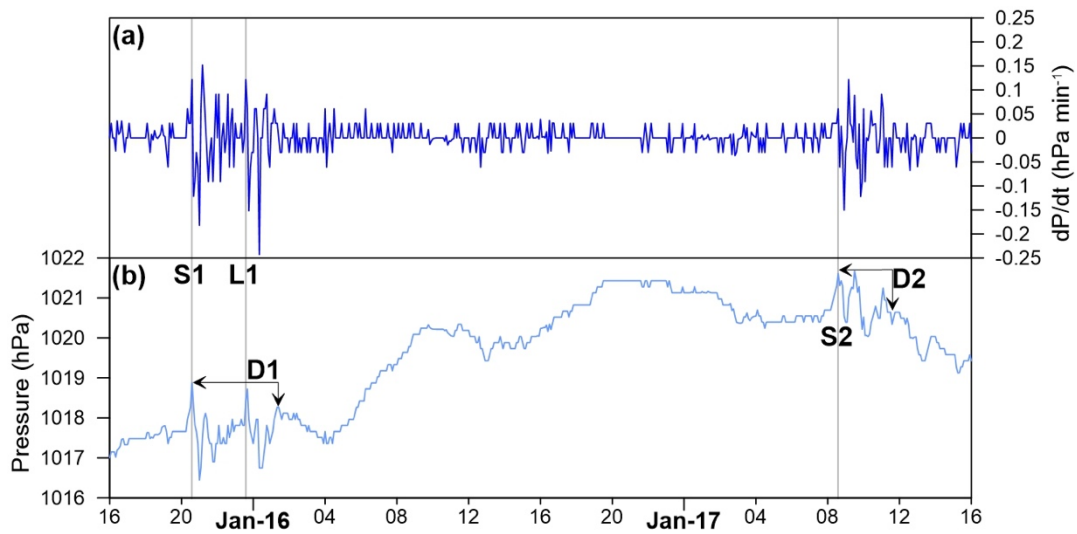


Figure 4. First time derivative (a) of the atmospheric pressure signal (b) recorded in the Palermo station of the SIAS network (Figure 1). First arrival times of the first (1) and second (2) passages of the shockwave travelling along the short (S) and long (antipodal, L) paths are indicated by the thin grey bars. The duration (D1,2) of the perturbations is also shown.

Compared to the pressure signal (Figure 4b), its first time derivative shows a richer, higher frequency content, but it is noisier, especially in the decaying coda.

According to the abovementioned characteristics, we picked the first arrival times using the first time derivative, while the durations were calculated on the pressure plot. Figure 5 reports the duration of the first and second passage of the shockwave plotted versus the latitude of the stations, expressing their progressive distances along the propagation direction of the perturbation. Pressure anomalies triggered by the first passage of the shockwave lasted 3–4 h, while those following the second passage show a much more variable duration, from a few tens of minutes to 4 h; the positive correlation between the duration and latitude will be discussed in the next chapter

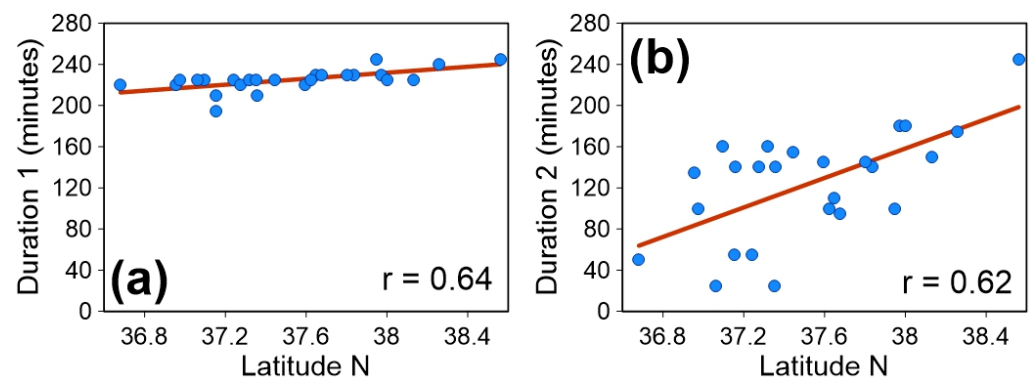


Figure 5. (a) Duration of pressure perturbations triggered by the first passage of the shockwave plotted versus latitude of the stations; (b) duration of pressure perturbations triggered by the second passage of the shockwave plotted versus latitude of the stations.

In both cases, the durations show a positive correlation with the geographical position of the stations, expressed as their latitude, with Pearson correlation coefficients greater than 0.6. To better investigate the spatial variations of the first arrival times of the Hunga shockwave and the duration of the consequent pressure perturbations, we plotted these in Figure 6 as isolines traced over the colour relief map of Sicily. The arrival times are reported as differences in minutes between each station and the first signal recorded by the network in the Salina island station (P47 in Figure 6a).

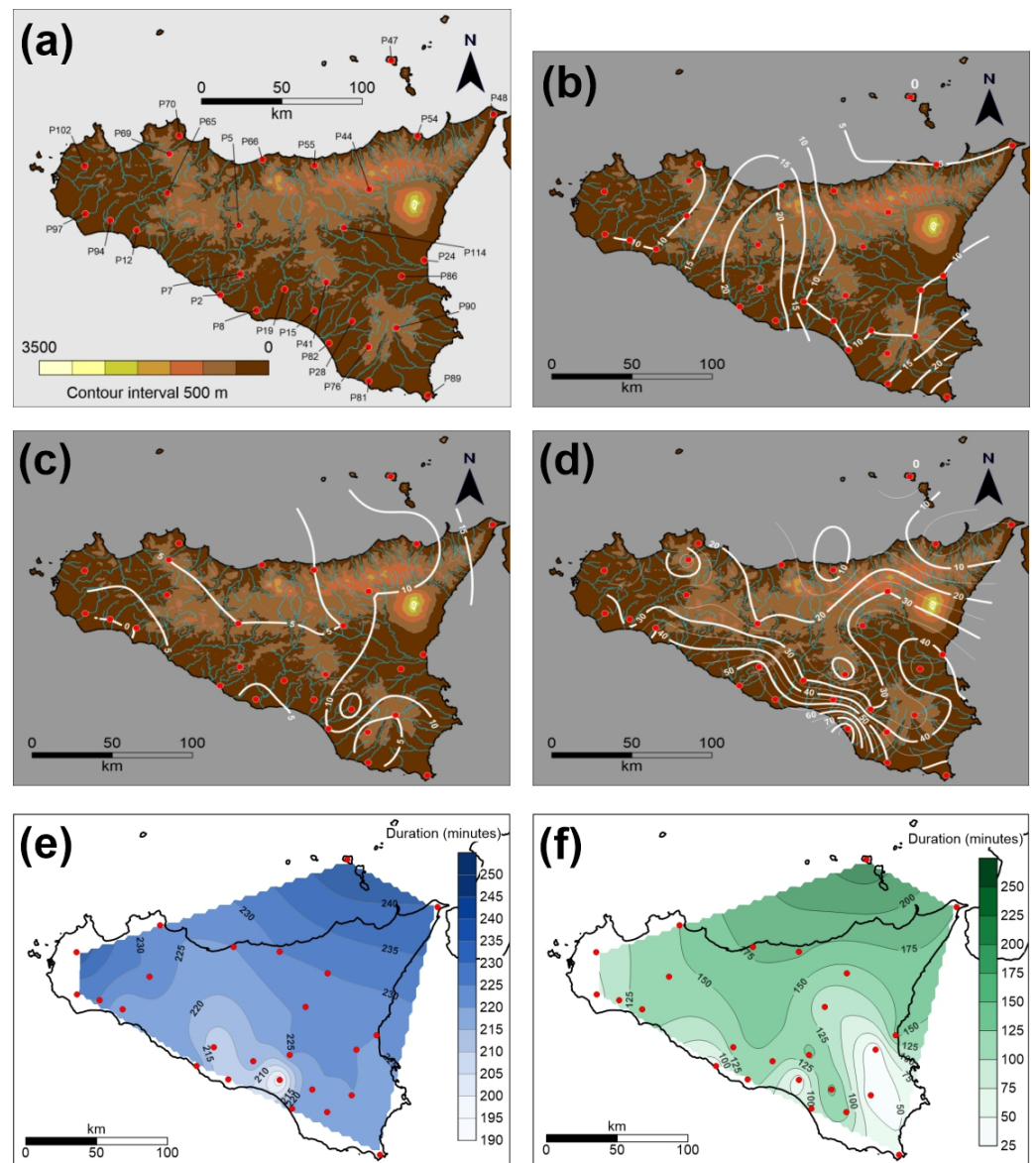


Figure 6. (a) Colour relief map of Sicily, with location of SIAS network stations (red circles) and main river network (light blue lines); (b) delay time (minutes) of the first atmospheric pressure anomaly onset (first passage of the shockwave along the short range); zero is the first detection time among the stations. See methods for details about the picking procedure. (c) Delay time (minutes) of the first atmospheric pressure anomaly onset (first passage of the shockwave along the long range); (d) delay time (minutes) of the first atmospheric pressure anomaly onset (second passage of the shockwave along the short range); (e) duration (minutes) of the instant atmospheric pressure anomaly (first passage, short and long ranges not discriminated); (f) duration (minutes) of the instant atmospheric pressure anomaly (second passage, short and long ranges not discriminated).

The first passage along the short range was from the north-east (Figure 6b) and travelled faster over the western and eastern sectors of Sicily than in its central part, corresponding to a north-south alignment created by the two main rivers of Sicily: the Imera Settentrionale (Northern) and Imera Meridionale (Southern) rivers. According to the opposite direction of the first antipodal passage, it travelled over Sicily from SW to NE and was faster than the direct one, with a maximum delay of 15 instead of 25 min (Figure 6c). Much more complex behaviour is shown by the second passage of the short-range shockwave (Figure 6d). It arrived from NE and travelled faster south-westward over the western sector of Sicily, where the topographic structure is more discontinuous and less elevated than in the eastern part.

In the east, the continuous topographic barrier, composed of the coastal chain of the Nebrodi and Peloritani Mts. (about 1800 m a.s.l. maximum elevation) and Mt. Etna (more than 3300 m a.s.l.), slowed the pressure perturbation (twice the travelling time recorded at the west). The interaction between two orthogonal propagation fronts seems to have affected the south-easternmost sector of Sicily, with the wavefront coming from NE disrupted by the ingression of a secondary one from NW to SE, and a consequent slowdown of the signal, with a maximum delay higher than 75 min on the south coast.

The last two panels illustrate the distribution of the duration of the baric perturbations triggered by the first (Figure 6e) and second (Figure 6f) passage of the Hunga shockwave. Their general behaviour is the same, with longer durations on the northern coast (see also Figure 5), but with a shorter minimum of the second passage (25 min) with respect to the first one (190 min), recorded in the same sector affected by the disruption of the NE wavefront previously described.

Other interesting features are found in analysing the vertical variations of the recorded signal. The amplitude of the perturbations was expressed as the maximum standard deviation of the pressure signal, calculated for 1 h time windows, and plotted in Figure 7a versus the elevation of the stations.

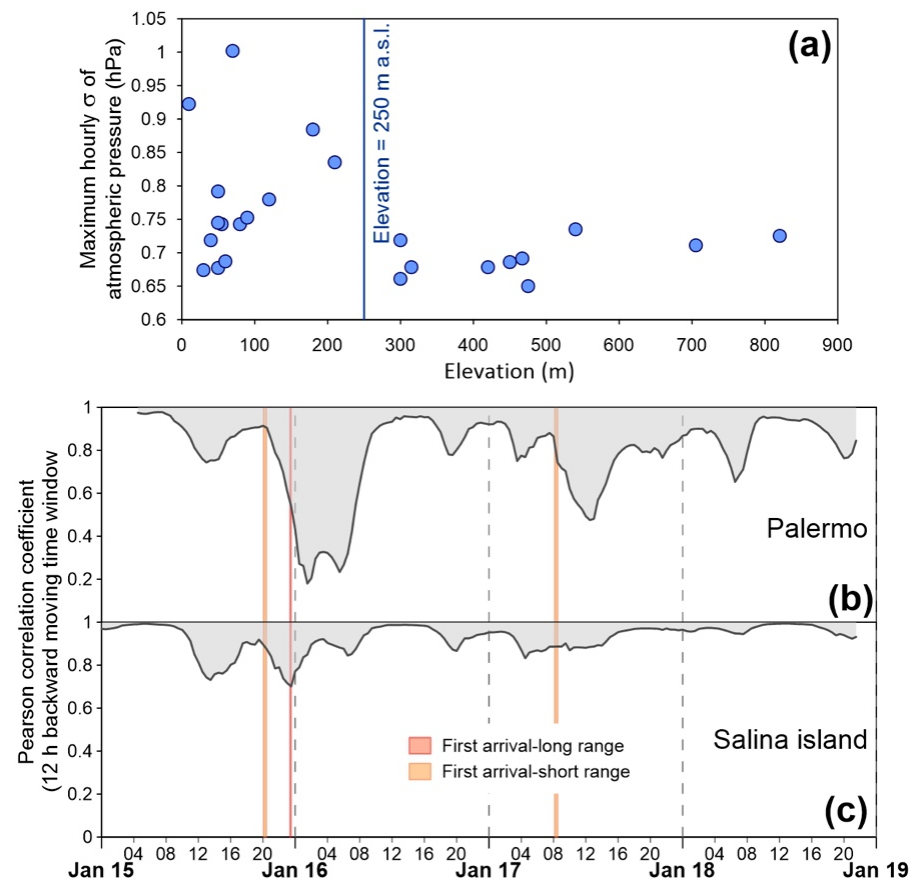


Figure 7. (a) Maximum hourly standard deviation (σ) of atmospheric pressure plotted versus elevation of the stations; (b) Pearson correlation coefficient of 30 min values of instant atmospheric pressure (12 h backwards moving time window) of the sea level station of the TROPOMAG network at Palermo, plotted versus the same data acquired at higher elevation; (c) the same data for Salina island. Vertical bars, as in Figure 3.

As shown in the figure, a marked difference exists between the stations located at elevations below and above 250 m a.s.l., respectively, with amplitudes variable in a range of 0.65–1 hPa for the former, and was compressed in a narrower band (0.65–0.75 hPa) for the latter.

Another way to investigate the vertical variations of pressure perturbations is the calculation of the Pearson correlation coefficients between contemporary data acquired in paired stations located at short distances but at significantly different altitudes [25]. This condition is specific for the TROPOMAG network (see methods), designed for investigating the atmospheric perturbances that are potentially induced by the geomagnetic activity, whose data are related to Palermo and Salina island (Figure 1) and are reported in Figure 7b,c. Decorrelations between the pressure signals acquired at Palermo, emerging from the background, strictly followed both the first and second passages of the shockwave, while no evidence of this phenomenon was recorded at Salina island.

Atmospheric pressure changes can also trigger the subsurface motion of gases in porous media; this phenomenon is known as “barometric pumping” [26] and specifically concerns transport by advection driven by a pressure gradient. The pressure gradient in the soil is given by the difference between the pressure of the gas source and the atmospheric one. If the gas source is at constant pressure, the gradient is controlled by the atmospheric pressure, whose variations can trigger changes in soil CO₂ emissions, as previously observed at Vulcano Island [27], and again after the passages of the Hunga shockwave, as illustrated in Figure 8.

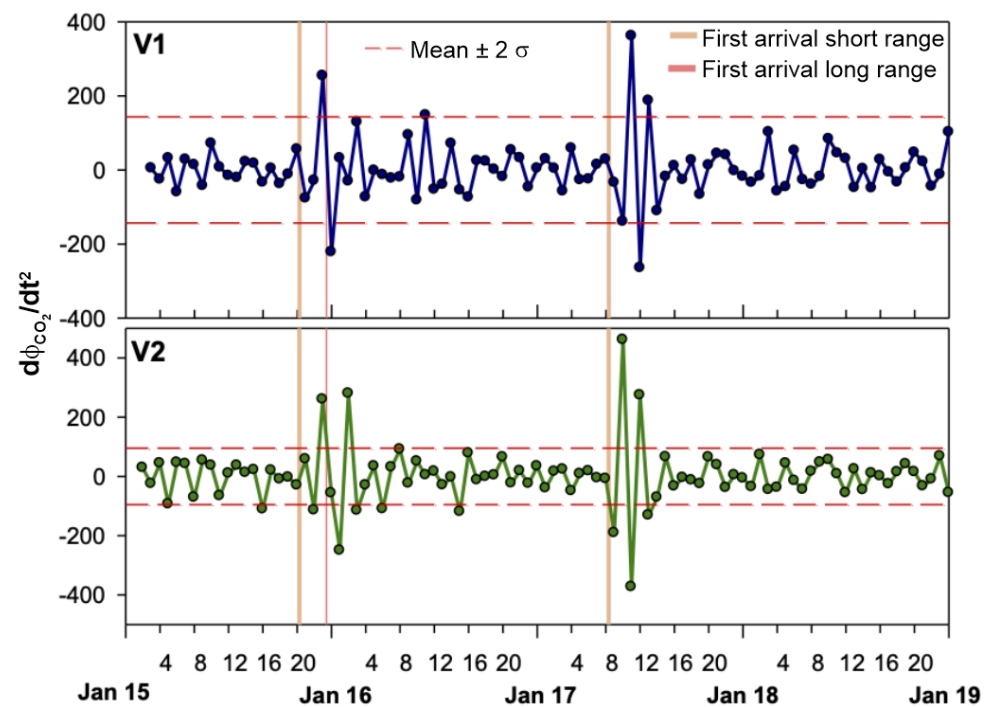


Figure 8. Second time derivative of hourly values of soil CO₂ flux (ϕ , $\text{g m}^{-2} \text{d}^{-1}$) measured in two monitoring stations (see methods) on the island of Vulcano (Figure 1), compared to its mean value $\pm 2\sigma$ for the considered period. First arrival times of the first and second passage of the shockwave travelling along the short and long ranges are also reported.

Here, the variability of the soil CO₂ flux is expressed using its second time derivative, for highlighting sudden changes, variable both in amplitude and sign, which is typical of turbulent conditions. As illustrated in the figure, shortly after the passages of the shockwave, the signal showed variations exceeding its mean value $\pm 2\sigma$ for the considered period.

3.3. Upper Atmosphere Response

Our regional analysis, based on both ionograms and TEC values, confirms what was found by other authors and shows that MSTIDs, related to the barometric variations triggered by the Hunga event, are clearly detected.

Figure 9a displays, in a travel time diagram, the detrended vertical TEC (dvTEC) (solid black lines) as measured by the selected RING stations (black dots in Figure 9b), as a function of both the universal time (UT) and the distance from the Hunga volcano.

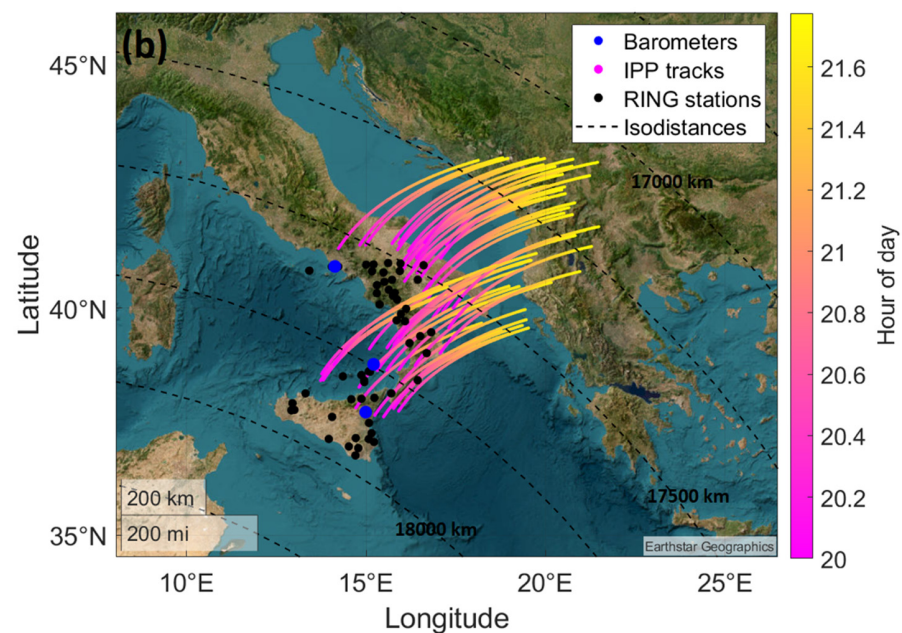
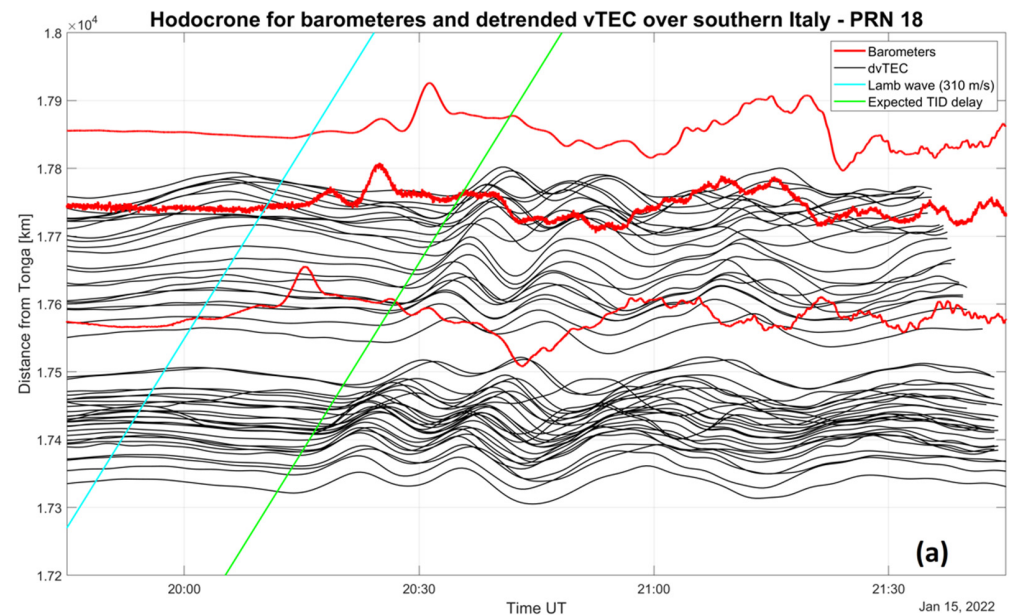


Figure 9. (a) dvTEC (solid black curves) as measured by RING GNSS stations from about 19:30 UT to 22 UT on 15 January 2022. The pressure variations (red curves) as registered by the barometers (red dots in Figure 2) described in the methods highlight the arrival of the neutral Lamb wave (cyan solid line), which propagates at 310 m/s, as found in Section 3.1. Respectively, from lower to higher distances from Hunga, the three barometers are located at Campi Flegrei, Stromboli and Etna. Moreover, one might notice how the signal gathered at Stromboli island shows a higher level of noise (making its red line appear thicker). The solid green line instead represents the expected TID arrival, which corresponds to 24 min after the neutral wave appearance. (b) Ionospheric pierce point (IPP) tracks from the different RING stations, in which colours represent the hour of the day. Dashed black curves represent the points with the same distance from the Hunga volcano. Black and blue dots represent, respectively, the location of GNSS receivers and barometers.

Specifically, the plot refers to the signal emitted from satellite G18 (PRN 18) and received from the selected RING receivers from 20 UT to 22 UT on 15 January 2022. The pressure variations (red lines), as registered by the barometric receivers, are also reported to highlight the arrival of the neutral Lamb wave. To better visualise the Lamb wave propagation in the lower atmosphere, the solid cyan line was added, representing the expected propagation of a Lamb wave that generated at the main eruption time and propagated at 310 m/s, as found in Section 3.1. The green line instead represents the expected time of arrival of the ionospheric disturbance, which is equal to the Lamb wave arrival time plus a certain delay. This delay is related to the vertical propagation of secondary waves generated by the passage of the Lamb wave, which propagates horizontally at the speed of sound from the source in the troposphere. From the literature [7,28], we know that each type of neutral wave (acoustic and gravity) is defined by a certain range of vertical propagation velocities and, therefore, different time delays between the appearance of the source of secondary waves (Lamb wave) at ground level and the ionised signature at the ionospheric shell height. For the slow, upward propagating gravity waves, the usual delay is around 45 min, while for the faster acoustic waves, this delay is normally about 10 min. This is further confirmed by the results of Matoza et al. [8], who found a time delay between the neutral and ion disturbances equal to 24 min over north-eastern Australia, and, therefore, we decided to use that same value as our expected time delay. Figure 9b also shows the ionospheric pierce point (IPPs) at 350 km (the assumed representative of the altitude of peak plasma density in the ionosphere) related to the considered RING stations, in which the colour bar is associated with the hour of the day.

The pressure waves measured at the three barometers (red curves) propagate at 310 m s^{-1} , which is in good accordance with the typical speed of sound at sea level. From $dvTEC$, two different wave-like perturbation patterns are visible with a delay, respectively, of 24 min (green line) and about 60 min, with respect to the neutral wave propagating at the ground. The first one, which is in good accordance with what was found by Matoza et al. [8] and was close to the antipode of southern Italy, corresponds to MSTIDs with a period of about 15/20 min and should be triggered by the propagation of secondary acoustic waves generated by the Lamb wave passage. The second one is again ascribable to MSTIDs, with a period of about 35/40 min, which, in this case, is likely to be the ionospheric manifestation of secondary gravity waves (GWs).

In order to look for the possible presence of ionospheric TIDs caused by gravity wave propagation induced by the first barometric variation recorded between about 20:12 UT and 20:36 UT (see Figure 9a), the ionogram traces recorded at Gibilmanna between 15 January 2022 at 18:00 UT and 16 January 2022 at 03:00 UT are also considered and manually digitised using the Interpre software [29]. This allows for obtaining pairs of (N, h') for each ionogram, where N is the electron density and h' is the virtual height of reflection.

Afterwards, using the POLAN technique [30], the inversion from the ionogram trace (N, h') to the vertical profile (N, h) , where h is the real height of reflection, is performed. From the obtained profiles (N, h) , one for each ionogram, the isoheight curves N ($h = \text{const} = 190, 200, 210, 220, 230, 240, 250, 260 \text{ km}$) are generated and plotted in Figure 10.

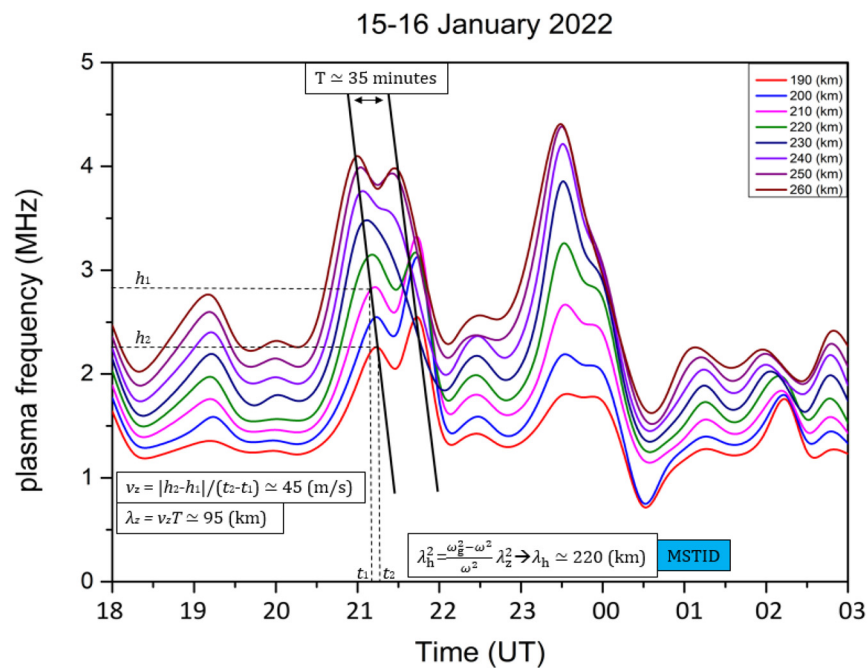


Figure 10. Electron density variations for the real height range of 190–260 km, computed between 15 January 2022 at 18:00 UT and 16 January 2022 at 03:00 UT. Oblique lines highlight the downward phase shift typical of gravity wave propagation.

The figure shows that from 21:00 UT to 22:00 UT, the maximum N variations occur first at 260 km and then at lower heights, highlighting a downward phase shift, which is characteristic of GW propagation in the ionospheric F region [31]. From the isoheight curves of Figure 10, it is possible to get an estimation of the GW period T equal to 35 min.

The vertical phase velocity, v_z , is calculated using the peak of two consecutive heights [32], and a value of $v_z \approx 45 \text{ m s}^{-1}$ is found; the vertical wavelength $\lambda_z = v_z T \approx 95 \text{ km}$ is then obtained. The corresponding horizontal wavelength (λ_h) can be determined using a relationship between λ_h and λ_z , given by Hines [31], namely, $\omega^2 \lambda_h^2 \approx (\omega_g^2 - \omega^2) \lambda_z^2$, where ω_g is the Brunt–Väisälä frequency, which was taken as $2\pi/14 \text{ min}^{-1}$ [33], and $\omega = 2\pi/T$ is the wave angular frequency. The horizontal wavelength comes out to be $\lambda_h \approx 220 \text{ km}$, which is a value consistent with an MSTID.

The same analysis done for the second barometric variation, recorded between 21:12 UT and 21:36 (see Figure 9), does not show any ionospheric signature of atmospheric wave propagation.

4. Discussion and Conclusions

Two passages of the Hunga shockwave over the Mediterranean were recorded by a multiparametric sensor network, sounding the atmosphere at different heights. Acquired data can be interpreted as a shock test, which is able to provide information on the atmospheric response, at the Earth’s scale, to short-lasting pressure transients such as those triggered by volcanic explosions.

The sampling period of barometric networks is often not appropriate for correctly detecting transients with high-frequency contents, such as the Hunga shockwave. The high-frequency (50 Hz) INGV barometric network, part of infrasonic and dilatometer volcanic surveillance systems, was detected as the first arrival of its lower frequency component at about 4.5 mHz, corresponding to a period of 3.7 min (Figure 2 and the related discussion). The other networks (Figures 1 and 3), implemented for meteorological measures, acquire data every 5 or 10 min, causing the aliasing of the recorded signal related to the passage of the Hunga shockwave (Figure 3). Although aliased, the barometric signals acquired at

5 min kept a sufficient frequency content for describing the space–time dynamics of the pressure disturbance over Sicily (Figures 4–6).

Under this focus, the passage of the Hunga shockwave can be interpreted as a stress test, sounding the efficiency of the barometric networks, at the global scale, for the correct detection of transients affecting small volumes of the 4D (space, time) space. These transients are typical of turbulent atmospheric conditions, ever more frequent due to the acceleration of weather phenomena caused by climatic changes; they require acquisition networks operating at high frequencies (Hz) and should be composed of paired stations at different altitudes with interspaces between adjacent stations of a few kilometres to be adequately recorded. Such conditions are typically found in the volcanic surveillance networks due to both the peculiar topographic structure of volcanoes (steep relieves with strong topographic gradients) and the impulsive nature of the phenomena to be recorded (volcanic explosions). On the opposite hand, barometric meteorological networks are commonly composed of single stations, interspaced over tens of kilometres and with acquisition rates of 5–10 min, which are inadequate for the detection of signals as those generated by the Hunga volcanic explosion.

Another relevant topic is the calculation of the travel velocity of the shockwave, differently estimated by various authors: 305 m s^{-1} by Chen et al. [5], 310 m s^{-1} in our study, and 315 m s^{-1} according to Harrison [9]. These velocities are compatible with those of the sound in the troposphere, at baric heights ranging between 4250 and 3350 m [34]. The middle-low troposphere was the fastest path for the shockwave propagation reasonably because, at these altitudes, there is an optimum between the upward decreasing sound velocity, due to both air rarefaction and cooling, and its downward decrease, due to the interference with the Earth's surface roughness. This last factor seems to play a fundamental role in the detection of the Hunga shockwave by ground-based barometric networks, as highlighted by the interpretation of the observations made in Sicily.

The first evidence is the dependence of the duration of pressure perturbations on the latitude of the recording stations, illustrated in the graph of Figure 5 and the maps of Figure 6e,f for both the first and second passages of the shockwave. The longer durations were detected in the north, with a progressive decrement moving southward, which was much more pronounced during the second passage. The direction and verses of these variations correspond to those of the altimetric profile of Sicily, characterised by a continuous mountainous chain immediately inland off its northern coast, with maximum elevations of 1800–2000 m above sea level, progressively degrading southward. Minor durations should be attributed to the destructive interferences exerted on the main wavefront moving from NE to SW by the secondary reflected and diffracted pressure waves originating from the interaction of the main baric front with the orographic structure.

Other observations support this interpretation. First of all, the dromochrones of the first arrival times of the direct (Figure 6b,d) and antipodal (Figure 6c) paths of the Hunga shockwave exhibit different behaviours. They show higher gradients along the direction of the direct path (from NE) and more variability along the transversal direction than the antipodal run (from SW), first impacting on low relieves, which progressively rise in elevation northward.

The vertical variability of the pressure signal is further confirmed by the analysis shown in Figure 7. The distribution of points in the barometric sensors' altitude versus the recorded signal's variability (expressed as its maximum hourly standard deviation) graph (Figure 7a) indicates that it was more stable and lower at elevations higher than 250 m than below this threshold. This behaviour suggests that the lower the detection point, namely into valleys surrounded by higher relieves, the more turbulent is the pressure signal due to the interferences from the secondary wavefronts reflected and diffracted by the orography. Another evidence of this phenomenon is given by the data shown in Figure 7b,c, which reports for Palermo city, but not at Salina island, a decorrelation of the atmospheric pressure signal recorded at different elevations. Namely, after the first direct passage of the Hunga

shockwave, the pressures recorded at different altitudes started varying independently of each other, resuming a simultaneous trend shortly after.

Concerning the ionospheric detection of the Hunga event, the corresponding analyses have been based on both the ionograms recorded at the Gibilmanna observatory and the calibrated TEC values retrieved by the GNSS receivers data of the RING network. The results showed that MSTIDs, which are strictly related to the barometric variations caused by the Hunga event, are clearly detected and well in accordance with what other authors have found. Specifically, the TEC analyses highlighted a first MSTID, with a period of about 15/20 min, which was most likely triggered by the upward propagation of secondary acoustic waves generated by the Lamb wave passage in the troposphere, which is fully consistent with the result by Matoza [8], and a second MSTID, with a period of about 35/40 min, which is almost certainly related to the propagation of secondary GWs generated in the lower atmosphere. In particular, this second wave phenomenon also emerges from the analysis of the ionograms from Gibilmanna, the results of which are well in agreement with those obtained on the TEC side, both in terms of the onset of the phenomenon and the period of the wave.

Finally, the impulsive changes in the soil CO₂ flux, recorded by two stations at Vulcano Island (Figure 8), reveal that pressure perturbations, triggered by the Hunga shockwave, affected even the lowest layers of the atmosphere and, here, slightly modified the emissions of volcanic CO₂ toward the atmosphere. This result suggests that two volcanoes, although located very far from each other, can interact via a pressure wave travelling in the lower troposphere and opens new perspectives on the way changes in the activity states of other volcanoes can modify volcanic gas emissions.

Author Contributions: Conceptualization, P.M.; methodology, P.M.; formal analysis, A.B. (Alessandro Bonforte), A.C., B.D.L., G.C., L.C., L.S., M.G., M.P., M.S., P.M. and P.R.; investigation, A.B. (Alessandro Bonaccorso), A.B. (Alessandro Bonforte), A.C., B.D.L., C.C., G.C., L.C., L.P., L.S., M.G., M.P., M.S., P.M., P.R. and S.D.G.; data curation, A.B. (Alessandro Bonaccorso), A.B. (Alessandro Bonforte), A.C., B.D.L., C.B., C.C., G.C., L.C., L.S., M.O., M.G., M.P., M.S., P.M., P.R., R.P., S.D.G. and V.R.; writing—original draft preparation, B.D.L., C.C., L.S., M.G., M.P., P.M. and S.D.G.; writing—review and editing, all authors. All authors have read and agreed to the published version of the manuscript.

Funding: This research was partially funded by the INGV Departmental Strategic Projects 2019 TROPOMAG.

Data Availability Statement: All relevant data are available from the authors on request.

Acknowledgments: This research is a part of the INGV Departmental Strategic Projects 2019 TROPOMAG. We wish to thank the technical staff of the INGV-OE infrasonic group for their support.

Conflicts of Interest: The authors declare no conflict of interest.

References

- Brenna, M.; Cronin, S.J.; Smith, I.E.M.; Pontesilli, A.; Tost, M.; Barker, S.; Tonga'onevai, S.; Kula, T.; Vaiomounga, R. Post-caldera volcanism reveals shallow priming of an intra-ocean arc andesitic caldera: Hunga volcano, Tonga, SW Pacific. *Lithos* **2022**, *412–413*, 106614. [[CrossRef](#)]
- Yuen, D.A.; Scruggs, M.A.; Spera, F.J.; Zheng, Y.; Hu, H.; McNutt, S.R.; Thompson, G.; Mandli, K.; Keller, B.R.; Wei, S.S.; et al. Under the surface: Pressure-induced planetary-scale waves, volcanic lightning, and gaseous clouds caused by the submarine eruption of Hunga Tonga-Hunga Ha'apai volcano. *Earthquake Res. Adv.* **2022**, *2*, 100134. [[CrossRef](#)]
- Carvajal, M.; Sepúlveda, I.; Gubler, A.; Garreaud, R. Worldwide signature of the 2022 Tonga volcanic tsunami. *Geophys. Res. Lett.* **2022**, *49*, e2022GL098153. [[CrossRef](#)]
- Xu, J.; Li, D.; Bai, Z.; Tao, M.; Bian, J. Large Amounts of Water Vapor Were Injected into the Stratosphere by the Hunga Tonga–Hunga Ha'apai Volcano Eruption. *Atmosphere* **2022**, *13*, 912. [[CrossRef](#)]
- Chen, C.-H.; Zhang, X.; Sun, Y.-Y.; Wang, F.; Liu, T.-C.; Lin, C.-Y.; Gao, Y.; Lyu, J.; Jin, X.; Zhao, X.; et al. Individual Wave Propagations in Ionosphere and Troposphere Triggered by the Hunga Tonga-Hunga Ha'apai Underwater Volcano Eruption on 15 January 2022. *Remote Sens.* **2022**, *14*, 2179. [[CrossRef](#)]
- Astafyeva, E.; Maletckii, B.; Mikesell, T.D.; Munaibari, E.; Ravanelli, M.; Coisson, P.; Manta, F.; Rolland, L. The 15 January 2022 Hunga Tonga eruption history as inferred from ionospheric observations. *Geophys. Res. Lett.* **2022**, *49*, e2022GL098827. [[CrossRef](#)]
- Astafyeva, E. Ionospheric Detection of Natural Hazards. *Rev. Geophys.* **2019**, *57*, 1265–1288. [[CrossRef](#)]

8. Matoza, R.S.; Fee, D.; Assink, J.D.; Iezzi, A.M.; Green, D.N.; Kim, K.; Toney, L.; Lecocq, T.; Krishnamoorthy, S.; Lalande, J.-M.; et al. Atmospheric waves and global seismoacoustic observations of the January 2022 Hunga eruption, Tonga. *Science* **2022**, *377*, 95–100. [[CrossRef](#)]
9. Harrison, G. Pressure anomalies from the January 2022 Hunga Tonga-Hunga Ha'apai eruption. *Weather* **2022**, *77*, 87–90. [[CrossRef](#)]
10. Wright, C.J.; Hindley, N.P.; Alexander, M.J.; Barlow, M.; Hoffmann, L.; Mitchell, C.N.; Prata, F.; Bouillon, M.; Carstens, J.; Clerbaux, C.; et al. Surface-to-space atmospheric waves from Hunga Tonga-Hunga Ha'apai eruption. *Nature* **2022**. [[CrossRef](#)]
11. Themens, D.R.; Watson, C.; Žagar, N.; Vasylykevych, S.; Elvidge, S.; McCaffrey, A.; Prikryl, P.; Reid, B.; Wood, A.; Jayachandran, P.T. Global propagation of ionospheric disturbances associated with the 2022 Tonga volcanic eruption. *Geophys. Res. Lett.* **2022**, *49*, e2022GL098158. [[CrossRef](#)]
12. Hines, C.O. An interpretation of certain ionospheric motions in terms of atmospheric gravity waves. *J. Geophys. Res.* **1959**, *64*, 2210–2211. [[CrossRef](#)]
13. Leitinger, R.; Rieger, M. The TID model for modulation of large scale electron density model. *Ann. Geophys.* **2005**, *48*, 515–523. [[CrossRef](#)]
14. Hong, J.; Kil, H.; Lee, W.K.; Kwak, Y.S.; Choi, B.K.; Paxton, L.J. Detection of different properties of ionospheric perturbations in the vicinity of the Korean Peninsula after the Hunga-Tonga volcanic eruption on 15 January 2022. *Geophys. Res. Lett.* **2022**, *49*, e2022GL099163. [[CrossRef](#)]
15. Verhulst, T.G.; Altadill, D.; Barta, V.; Belehaki, A.; Burešová, D.; Cesaroni, C.; Galkin, I.; Guerra, M.; Ippolito, A.; Herekakis, T.; et al. Multi-instrument detection in Europe of ionospheric disturbances caused by the 15 January 2022 eruption of the Hunga volcano. *J. Space Weather Space Clim.* **2022**, *12*, 35. [[CrossRef](#)]
16. Buonocunto, C.; D'Auria, L.; Caputo, A.; Martini, M.; Orazi, M. The InfraCyrus infrasound sensor. *Rapp. Tec. INGV* **2011**, *188*, 5–12.
17. Baskaradas, J.A.; Bianchi, C.; Pezzopane, M.; Romano, V.; Sciacca, U.; Scotto, C.; Tutone, G.; Zuccheretti, E. New Low Power Pulse Compressed Ionosonde at Gibilmanna Ionospheric Observatory. *Ann. Geophys.-ITALY* **2005**, *48*, 445–451. [[CrossRef](#)]
18. Upper atmosphere physics and radiopropagation Working Group; Marcocci, C.; Pezzopane, M.; Pica, E.; Romano, V.; Sabbagh, D.; Scotto, C.; Zuccheretti, E. Electronic Space Weather upper atmosphere database (eSWua)—HF data, version 1.0. *Ist. Naz. Geofis. Vulcanol. (INGV)* **2020**. [[CrossRef](#)]
19. RING—Rete Integrata Nazionale GNSS. Available online: <https://ring.gm.ingv.it> (accessed on 23 November 2022).
20. Ciralo, L.; Azpilicueta, F.; Brunini, C.; Meza, A.; Radicella, S.M. Calibration errors on experimental slant total electron content (TEC) determined with GPS. *J. Geod.* **2007**, *81*, 111–120. [[CrossRef](#)]
21. Cesaroni, C.; Spogli, L.; De Franceschi, G. IONORING: Real-Time Monitoring of the Total Electron Content over Italy. *Remote Sens.* **2021**, *13*, 3290. [[CrossRef](#)]
22. Camarda, M.; Gurrieri, S.; Valenza, M. CO₂ flux measurements in volcanic areas using the dynamic concentration method: Influence of soil permeability. *J. Geophys. Res.* **2006**, *111*, B05202. [[CrossRef](#)]
23. Press, F.; Harkrider, D. Propagation of acoustic-gravity waves in the atmosphere. *J. Geophys. Res.* **1962**, *67*, 3889–3908. [[CrossRef](#)]
24. Pierce, A.D.; Posey, J.W.; Iliff, E.F. Variation of nuclear explosion generated acoustic-gravity wave forms with burst height and with energy yield. *J. Geophys. Res.* **1971**, *56*, 5025–5042. [[CrossRef](#)]
25. Madonia, P.; Romano, P.; Inguaggiato, S. Decoupling of ground level pressures observed in Italian volcanoes: Are they driven by space weather geo-effectiveness? *Ann. Geophys.* **2014**, *57*, S0324. [[CrossRef](#)]
26. Auer, L.H.; Rosenberg, N.D.; Birdsell, K.H.; Whitney, E.M. The effects of barometric pumping on contaminant transport. *J. Contam. Hydrol.* **1996**, *24*, 145–166. [[CrossRef](#)]
27. Camarda, M.; De Gregorio, S.; Capasso, G.; Di Martino, R.M.R.; Gurrieri, S.; Prano, V. The monitoring of natural soil CO₂ emissions: Issues and perspectives. *Earth Sci. Rev.* **2019**, *198*, 102928. [[CrossRef](#)]
28. Savastano, G.; Ravanelli, M. Real-Time Monitoring of Ionospheric Irregularities and TEC Perturbations. In *Satellites Missions and Technologies for Geosciences*; Demyanov, V., Becedas, J., Eds.; IntechOpen: London, UK, 2019. [[CrossRef](#)]
29. Pezzopane, M. Interpret: A Windows software for semiautomatic scaling of ionospheric parameters from ionograms. *Comput. Geosci.* **2004**, *30*, 125–130. [[CrossRef](#)]
30. Titheridge, J.E. The real height analysis of ionograms: A generalized formulation. *Radio Sci.* **1988**, *23*, 831–849. [[CrossRef](#)]
31. Hines, C.O. Internal atmospheric gravity waves at ionospheric heights. *Can. J. Phys.* **1960**, *38*, 1441–1481. [[CrossRef](#)]
32. Pezzopane, M.; Fagundes, P.R.; Ciralo, L.; Correia, E.; Cabrera, M.A.; Ezquer, R.G. Unusual nighttime impulsive foF2 enhancement below the southern anomaly crest under geomagnetically quiet conditions. *J. Geophys. Res.* **2011**, *116*, A12314. [[CrossRef](#)]
33. Abdu, M.A.; Batista, I.S.; Kantor, I.J.; Sobral, J.H.A. Gravity wave induced ionization layers in the night F-region over Cachoeira Paulista (22° S, 45° W). *J. Atmos. Terr. Phys.* **1982**, *44*, 759–767. [[CrossRef](#)]
34. Kirtskhalia, V.G. Speed of Sound in Atmosphere of the Earth. *Open J. Acoust.* **2012**, *2*, 80–85. [[CrossRef](#)]

Disclaimer/Publisher's Note: The statements, opinions and data contained in all publications are solely those of the individual author(s) and contributor(s) and not of MDPI and/or the editor(s). MDPI and/or the editor(s) disclaim responsibility for any injury to people or property resulting from any ideas, methods, instructions or products referred to in the content.